2003-07-09

Multienergetic External-beam PIXE as a Means of Stydying the Surface Enrichment Effect in Coins

Scott Evans Perry
Brigham Young University - Provo

MULTIENERGETIC EXTERNAL-BEAM PIXE AS A MEANS OF STUDYING THE SURFACE ENRICHMENT EFFECT IN COINS

by

Scott E. Perry

A thesis submitted to the faculty of

Brigham Young University

in partial fulfillment of the requirements for the degree of

Master of Science

Department of Physics and Astronomy

Brigham Young University

August 2003

BRIGHAM YOUNG UNIVERSITY

GRADUATE COMMITTEE APPROVAL

of a thesis submitted by

Scott E. Perry

This thesis has been read by each member of the following graduate committee and by majority vote has been found to be satisfactory.

Date	Lawrence B. Rees, Chair
Date	Nolan F. Mangelson
Date	Steven E. Jones

BRIGHAM YOUNG UNIVERSITY

As chair of the candidate's graduate committee, I have read the dissertation of Scott E. Perry in its final form and have found that (1) its format, citations, and bibliographical style are consistent and acceptable and fulfill university and department style requirements; (2) its illustrative materials including figures, tables, and charts are in place; and (3) the final manuscript is satisfactory to the graduate committee and is ready for submission to the university library.

_____
Date

_____
Lawrence B. Rees
Chair, Graduate Committee

Accepted for the Department

_____
R. Steven Turley, Chair
Department of Physics and Astronomy

Accepted for the College

_____
G. Rex Bryce, Associate Dean
College of Physical and Mathematical Sciences

ABSTRACT

MULTIENERGETIC EXTERNAL-BEAM PIXE AS A MEANS OF STUDYING THE SURFACE ENRICHMENT EFFECT IN COINS

Scott E. Perry

Department of Physics and Astronomy

Master of Science

This thesis paper examines the feasibility of using external-beam PIXE to study the surface enrichment effect in metal artifacts. By varying the energy of the incident proton beam, we penetrated the artifact's surface to different levels and were able to produce a depth profile of the elemental composition of the sample. In this study, the sample set we chose to examine consisted of ancient and modern coins.

This paper first describes the surface enrichment effect and theoretically how PIXE can be used to study it. It then details the construction of the components of the external-beam setup. Many of the refinements of the hardware and experimental methods are discussed. It recounts the means of calibration of the detector and analytical tools. Finally, an accounting of the research performed on several coins is set forth, along with

data showing the effectiveness of PIXE in complementing other methods of elemental analysis.

We found that PIXE revealed statistically significant differences in concentrations of modern coins at the two beam energies we used. Ancient coins did not have similarly significant discrepancies between the two beam energies. The modern coin data suggested depletion in copper in copper-silver and copper-gold alloys, which is consistent with predictions of the theory of the surface enrichment effect. We suggest that the ancient coins are so deeply corroded that the PIXE beam is unable to penetrate adequately to observe surface enrichment. Comparison of our PIXE data to XRF and SEM data suggest that the trends we observed in modern coins are verified by the other methods. We therefore assert that external-beam PIXE is an effective tool for studying the surface enrichment effect, though with the beam energies available at Brigham Young University, the study must be limited to fairly modern coins.

ACKNOWLEDGEMENTS

Many people have made significant contributions to this research project, both through direct and indirect support. Dr. Rees and Dr. Mangelson have worked countless hours striving to assure the quality of the research, even though our findings were limited by time constraints placed upon us by the accelerator. The have generously provided beam time and research funds to promote the success of this project. Most of all, they have patiently guided an inexperienced and often simple-minded graduate student without begrudging any of their time.

From the Department of Physics and Astronomy, Wes Lifferth has been a praiseworthy collaborator in the construction of all of the hardware in our experiment. He too has exhibited great patience in being asked to perform very difficult tasks and has remained as friendly as when I first met him. Joseph Young and Scott Daniel have devoted a great deal of effort to repairing the machine. Scott Sommerfeldt and Robert Turley have also patiently continued my funding to allow me to complete this thesis paper.

My family members have encouraged me and in many ways have made it possible for me to complete this research. My parents and my wife deserve my special thanks for their faith, love, patience, and help in seeing this project through to the very end.

TABLE OF CONTENTS

LIST OF FIGURES AND TABLES

CHAPTER I

INTRODUCTION AND BACKGROUND

PIXE has become a widely recognized method of chemical analysis because of its simplicity, accuracy, and nondestructive nature. Its name describes the physical principles behind its functioning: PIXE is an acronym for proton-induced x-ray emission.[1] Protons accelerated into a sample pull inner-shell electrons out of their orbitals. Outer electrons replenish the inner shells, but in order to drop to the lower-energy orbital, they emit the energy difference in the form of X rays. Each element has a unique set of atomic energy levels, therefore each element has a unique spectrum of x-ray emission. A large number of emissions from a particular transition will produce a peak in the spectrum, thereby identifying the existence of a species of atom in the sample. By analyzing the x-ray spectrum of a sample under proton bombardment, one can deduce which elements are present and what their concentrations are (see Figure 1).

Elements with an atomic number up to fifty (tin) are revealed by their K-series emissions, or transitions to the first (n=1) energy level. Beyond tin, the K series is too energetic for our detectors, so we instead look for the L series, or transitions to the second (n=2) energy levels. Guelph's GUPIX software analyzes spectra and reports the concentrations of elements in the sample.[2] In order for GUPIX to provide an accurate report, it must be given information about the sample's composition, the geometry of

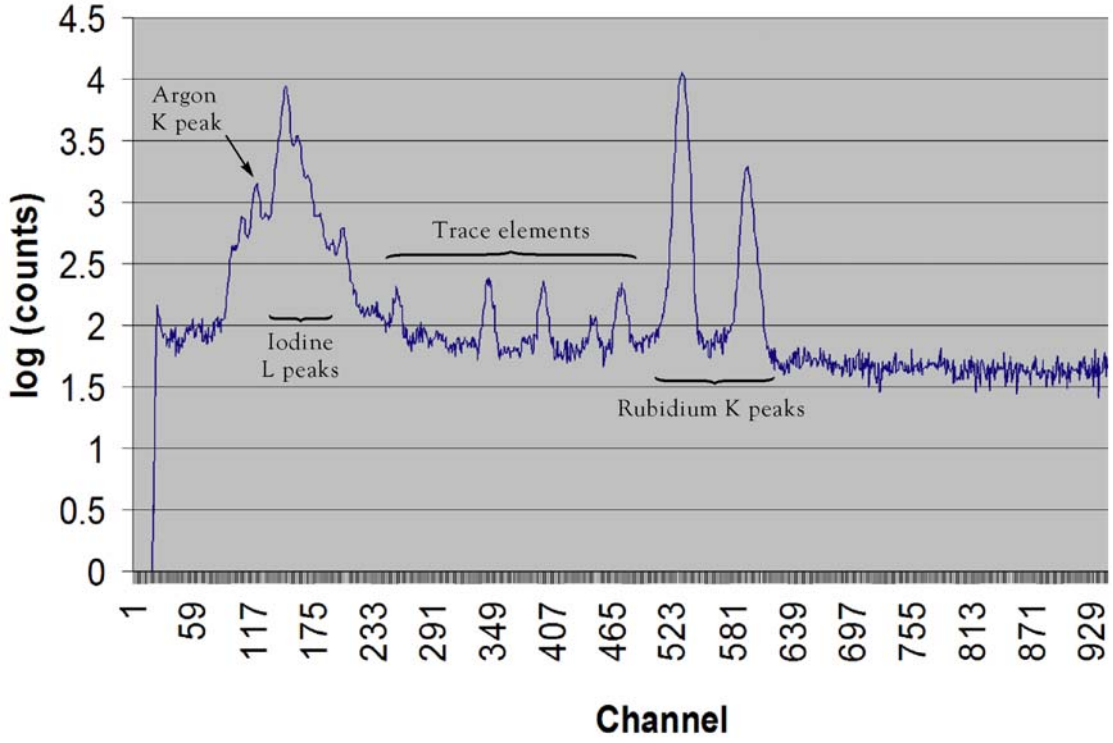

Figure 1: Sample spectrum taken from the RbI standard

the PIXE setup, the detector's specifications, the beam energy, and the total quantity of charge deposited by the beam.

Several pieces of equipment are needed to carry out PIXE analysis (see Figure 2). Obviously, a proton accelerator and an x-ray detector are essential to the operation of a PIXE system. An evacuated beamline is needed to guide the beam from the accelerator to the target. The steering electromagnet serves two purposes: it allows one accelerator to be permanently attached to several different beamlines and makes the beam monoenergetic. The degree of deflection of a beam of charged particles in a magnetic field depends on the momentum of the particles. If a particle has more or less kinetic energy than the desired beam, it will not turn with the same radius of curvature when it

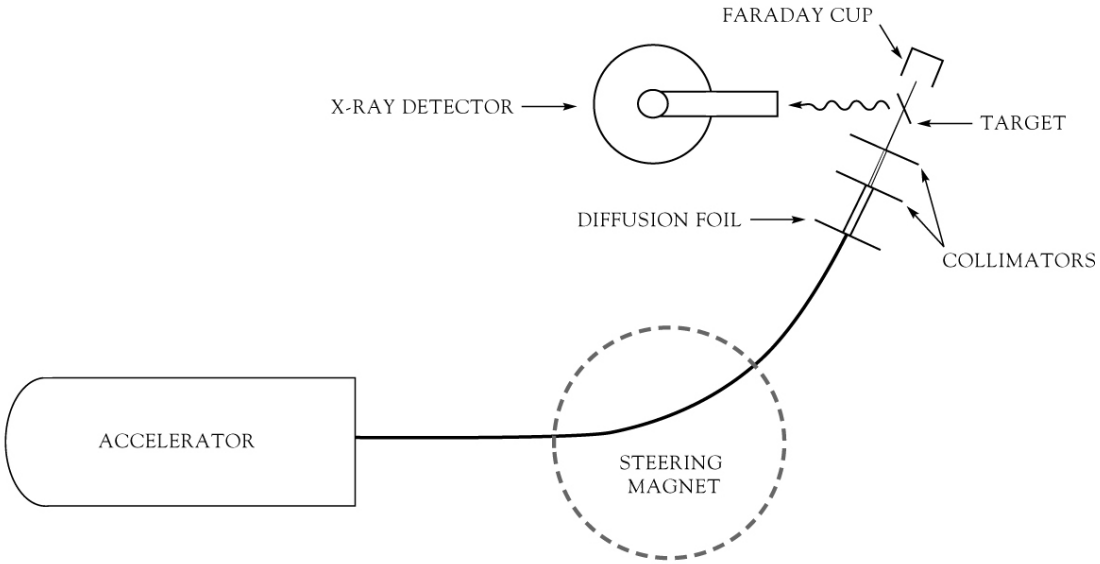

Figure 2: Schematic diagram of a PIXE setup

passes through the magnet and will not enter the correct beamline. In this way, the magnet assures that the beam that progresses to the target is nearly monoenergetic. Another aid in this regard is a set of collimators, which block particles with a trajectory other than parallel to the beamline axis, such as ones that have a close enough energy to pass through the steering magnet, but do not travel straight down the beamline. They also reduce the beam to the desired size.

Further refinement to the beam is possible through the use of a diffusion foil. Usually a thin graphite layer, the diffusion foil spreads the beam. This reduces the beam's intensity and makes it more uniform over its cross section. The beam is usually collimated after diffusion to achieve the desired beam diameter. After the beam has reached the target, it is collected in a Faraday cup, which stops the beam and measures the beam current. The Faraday cup is connected to a current integrator, or scaler, which measures how many beam particles pass through the sample.

A special application of PIXE is external-beam PIXE, in which the proton beam leaves the evacuated beamline and proceeds through a gaseous medium to the target.[1] A beam snout that terminates with a Kapton-foil window is a necessary addition to the beam line for external-beam PIXE. The Kapton allows protons to pass with a small decrease in energy, but it maintains a barrier to separate the atmospheric pressure of the lab from the very low vacuum inside the beamline.[1]

External-beam PIXE offers many advantages over standard PIXE, such as the ability to analyze large or irregularly shaped samples that otherwise could not be put into the evacuated target chamber. It also aids in making the bombardment of the sample less destructive because convection cools the sample. Another destructive situation develops in standard PIXE when charge builds up in the sample. If the sample is electrically isolated, the constant bombardment by protons produces a net positive charge in the sample. The Coulomb repulsion from these charges can cause spontaneous releases of charge, which often damage the sample and produce a large x-ray background in spectra. Charge buildup on the sample is less of a concern with external-beam PIXE because the atmosphere allows charges to escape in a slow, controlled manner. A helium atmosphere is particularly well-suited for external-beam PIXE because the helium atoms efficiently remove heat from the sample, they do not react with the sample, they do not rob the beam of as much energy as heavier gases, and none of the helium spectrum is detectable by the x-ray detectors used in PIXE.

Previously an external-beam PIXE apparatus was built and tested at Brigham Young University. It proved to be functional, as was demonstrated by the successful analysis of a bronze artifact from the Foundation for Ancient Research and Mormon Studies (FARMS).[3] The system was, however, not fully calibrated or refined, and many components needed upgrading to make the conditions of analysis more reproducible. One of our main goals in this research was to make the external-beam PIXE system at the university more streamlined, safer for samples, and more accurate through a careful calibration of the entire system.

While researching articles prior to the first external-beam PIXE project, we encountered many references to surface enrichment in archeometric PIXE studies with metal alloys. Demortier and Meyer and Brissaud's team observed silver enrichment in their respective studies of medieval and Gaulish coins.[4,5] The Portuguese team of Araujo, Alves, and Cabral also reported surface enrichment in gold coins when they compared their PIXE data to x-ray fluorescence (XRF), which penetrates deeper into the coin.[6] Clues to the cause of surface enrichment are found in *Methods of Chemical and Metallurgical Investigation of Ancient Coinage*, published by the Royal Numismatic Society.[7] They give the two main causes of silver enrichment in silver-copper alloys as oxidation of copper and the resulting relief of silver structures after the coin is cleaned. Evidently the copper oxide is removed from the surface with other crustal deposits, leaving a larger fraction of silver behind. A third cause of surface enrichment is "the redeposit of silver which replaces more or less completely the grains of copper oxide in

the vicinity of the surface."[7] This appears only in highly oxidized coins, such as ones left to great exposure to the elements.

The kinetic energy of the protons is critical to the depth to which the beam penetrates a sample. As the protons pass through a material, they gradually lose energy to interactions with the other charged particles in the substance. At a certain depth, nearly all of the energy is given up and the beam stops. When this happens within the target, it is called "thick", while if the beam passes through the target and continues beyond it, it is referred to as "thin". In the case of thick targets, the depth at which most of the beam stops is determined by the initial energy of the protons. In general, a higher beam energy corresponds to a greater depth at which the protons cause x-ray fluorescence. In this way, varying the energy of the beam affects the depth at which a thick sample's composition is analyzed. Depending on the sample's composition, some of the X rays may be absorbed by the material before they reach the detector. Gratefully, GUPIX accounts for this absorption when it analyzes the spectrum. Thus PIXE bears some advantages over XRF; only ion beams can select a preferential depth of analysis in a thick target.

Other researchers have capitalized on the finite penetration of proton beams to study the concentration of samples at varying depths. Early work in the theory and the proof of principle of this method was conducted respectively by Jaksic, et al, and Brissaud, et al.[8,9] Since then, more papers have appeared which utilize PIXE depth profiling as a means of analysis. Some researchers have used PIXE as one phase in a multifaceted

analytical system involving several methods.[10] They have nearly all chosen to vary the energy of their proton beam, though a similar effect can be achieved by varying the angle of incidence of a single-energy beam.[11]

Interestingly, in publications regarding PIXE studies of metal artifacts, surface enrichment is nearly always cited as a source of uncertainty in the findings. It does not appear that any research has been done to better determine the circumstances surrounding surface enrichment or whether an understanding of the surface enrichment effect might yield information about many of these metal samples. We therefore determined we would study the surface enrichment effect in coins with multienergetic, external-beam PIXE as a means of depth profiling. We hoped to link the extent of surface enrichment to factors surrounding the origin of the coin.

External-beam PIXE is well-suited to the analysis of coins for many reasons. The depth of penetration is well-defined, so the sample can be analyzed at several different beam energies with little chance of overlap in the depth of analysis. The energy of the beam can be changed relatively easily, as can the region that is being analyzed on the surface of the coin. Based on our research in the literature, it appeared that PIXE's range of depth within the sample would allow us to study the surface enrichment effect. Finally, external-beam PIXE is by nature nondestructive, which is especially important for the analysis of valuable coins and artifacts.

Valuable coins require special considerations which are answered by external-beam PIXE. Because the analysis may be performed on the coin in its entirety, no sample of the alloy must be removed for PIXE. Heat buildup is also averted by the use of an external-beam with a helium atmosphere. Charging of the sample does not occur because most coins are conductors. If the coin is grounded, PIXE will not deposit charge in the target more rapidly than it can be dissipated. Thus, we needed a target holder that would ground the coin and hold it securely without endangering it to scratching. Finally, the analysis must be accurate to make it worthwhile for a collector to release the coin to us for examination.

Our objective in undertaking this research was to establish a means of depth profiling with external-beam, multienergetic PIXE while observing the requirements for valuable samples listed above. We were required to modify and test the external-beam apparatus, calibrate our analytical tools, and verify our ability to observe surface enrichment in actual samples. We then assessed our ability to apply our findings of the surface enrichment effect as a potential tool for the study of coins and other metallic samples at Brigham Young University. The following chapters describe the preparations and methods that brought us to our results, which will then be discussed.

CHAPTER II

PREPARATIONS

Before we were able to collect spectra, we had to make a number of changes to the existing external-beam apparatus. Considerable testing went into determining what we needed for equipment so that we could obtain reliable and reproducible results. We also performed tests to improve our knowledge of the behavior of the machine and the samples during the testing process.

One of the first tests we performed as part of this thesis research was to determine whether external-beam PIXE is actually nondestructive. Visual inspection of samples analyzed with PIXE did not reveal any sort of surface marring, even under magnification, so we chose to use electron microscopy to search for evidence of damage. Among the coins selected for this study were 1-cent and 25-cent proof coins, uncirculated quarters and cents, and an ancient bronze. Predetermined regions of the coins were examined with the electron microscope. Images from the initial scans were saved for later comparison. The coins were then placed in the external beam where they were bombarded with maximum-energy protons at high beam currents. This was done to simulate the harshest conditions to which they could be subjected in our lab. Some coins were grounded, and some were not. All were run with a helium flow directed on their surface. The same regions of the coins were then reexamined with the electron

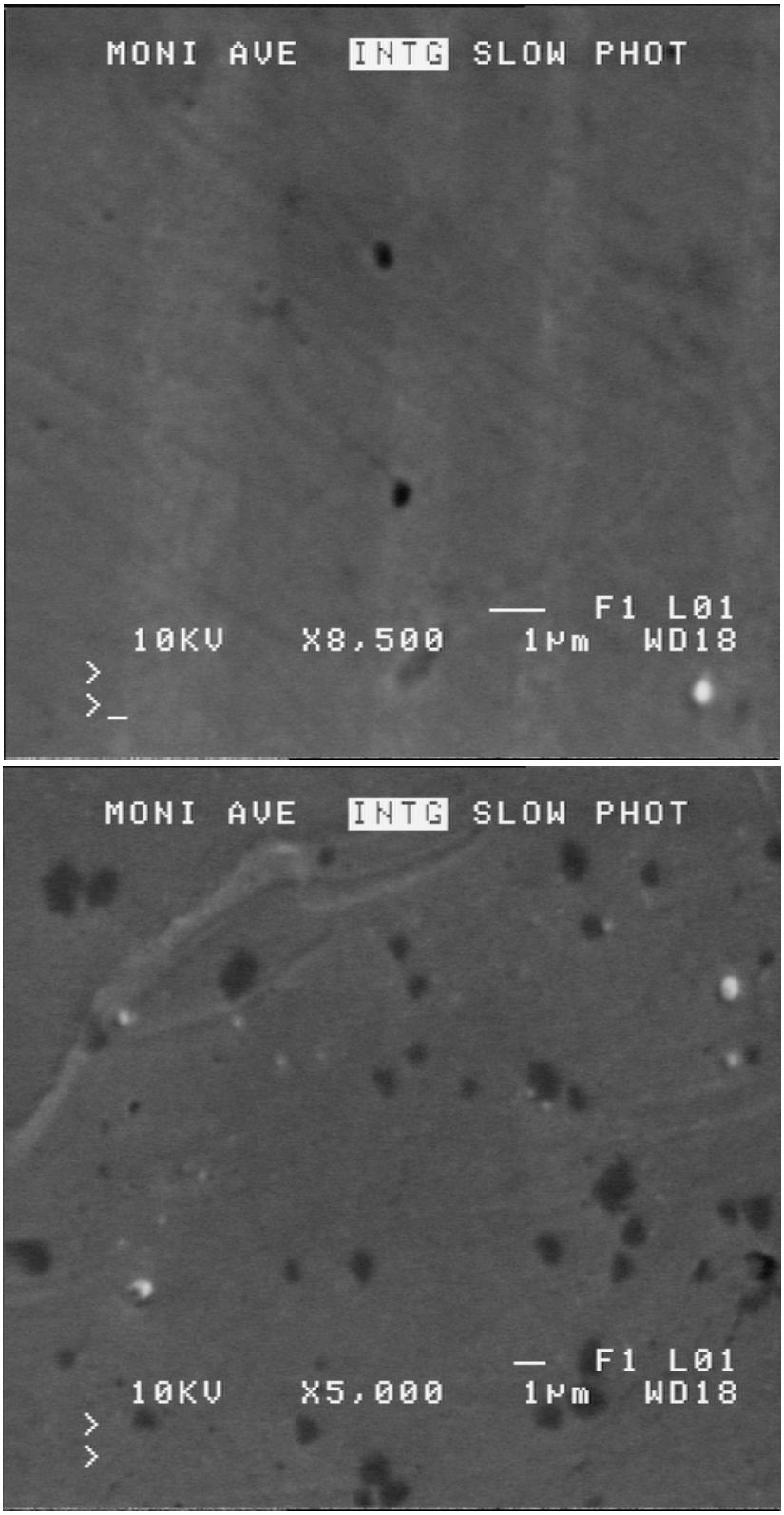

Figure 3: Electron micrographs of pitting in silver (above) and copper (below)

microscope. It was found that the exceptionally smooth surfaces of the proof coins exhibited pitting, which was probably caused by the proton beam (see Figure 3). The pits had a diameter of approximately one micron in copper, less than one micron in silver. The pits in the copper were spaced more closely than those in silver. Marring appeared to occur regardless of whether the coin was grounded while in the proton beam. Pits also appeared on the uncirculated coins after being bombarded by protons, though their presence was not as obvious because of the relative coarseness of their surface. The surfaces of the bronze coins were so coarse that no real change in surface texture could be observed after exposure to the proton beam (see Figure 4). In all three cases, it would appear that the same pitting occurred, but the effect was hardly

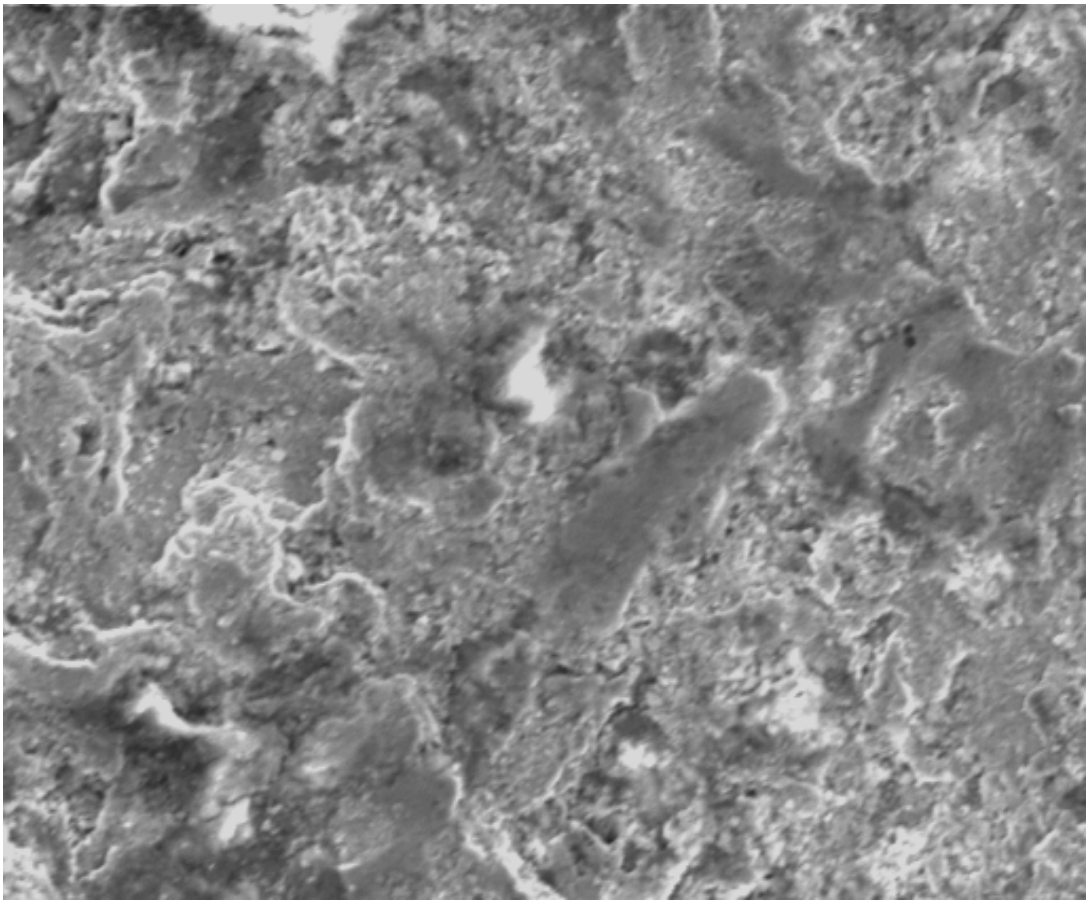

Figure 4: Roman bronze coin after beam exposure, 1000x magnification

noticeable in coins that were no longer in mint condition. Therefore, even though the method appears to cause some microscopic damage to the surface of metals, this should not be a concern except when analyzing uncirculated coins and artifacts.

Another important step we performed outside of the lab before beginning to experiment was to estimate of the beam energy at the target. As a proton beam passes through matter, its intensity is not significantly attenuated, but it loses some energy due to interactions with the charged particles in the matter's atoms. Once the beam's energy has dropped to a certain value, the protons lose the remainder of their energy. This causes the beam to stop at a fairly well-defined depth which is determined by the elements in the sample and the energy of the beam when it reaches the sample's surface. GUPIX accounts for x-ray attenuation in the sample, however it requires an accurate input of the beam energy at the surface of the target so that it can calculate the depth at which the characteristic X rays originate. Therefore, in order for an accurate GUPIX analysis of a thick-target spectrum, it is very important to know the energy of the beam when it impinges on the surface of the sample.

We therefore attempted to accurately measure the properties of the matter that the beam would encounter after passing through the steering magnet. The graphite diffusion foil was weighed and its cross-sectional area was found to determine its thickness. Since the graphite has a density of 1.5 g/cm^3, we calculated the thickness to be 7.33 μm.[12] The thickness of the Kapton foil, 8.47 μm, was calculated according to the nominal thickness printed on the roll from which it was taken. The distance from the end of the

beam snout to the intended location of the target was also carefully measured. Throughout this part of the beam's path, the protons would have to pass through the atmosphere in the target chamber.

To determine the composition of the gas in the target chamber during operating conditions, we exploited the presence of argon in air. With the proton beam entering laboratory air in the target chamber, we recorded a spectrum for a certain period of time. We then pumped the air out of the chamber and replaced it with helium gas. Another spectrum was captured over the same time interval. We compared the area under the argon peak in the air spectrum to the area in the helium spectrum to determine approximately what fraction of air remained after the chamber had been filled with helium. We concluded the following composition of the chamber atmosphere, by nucleus: 99.727% He, 0.2136% N, 0.0573% O, 0.0018% Ar. All of the values for the various thicknesses were then put into a Matlab program to calculate the beam energy loss as it passes through a material. The initial energy values were calculated according to the field strength of the steering magnet when the beam entered the beamline correctly. The values we obtained through use of this Matlab code provided a starting point for more elaborate calculations of the beam energy at the target, which will be described later.

Several important pieces of hardware needed to be incorporated into our apparatus (see Figure 5). For our target chamber, we chose a large, round vacuum chamber that had formerly been used with Rutherford backscattering (RBS) studies. The airtight seal

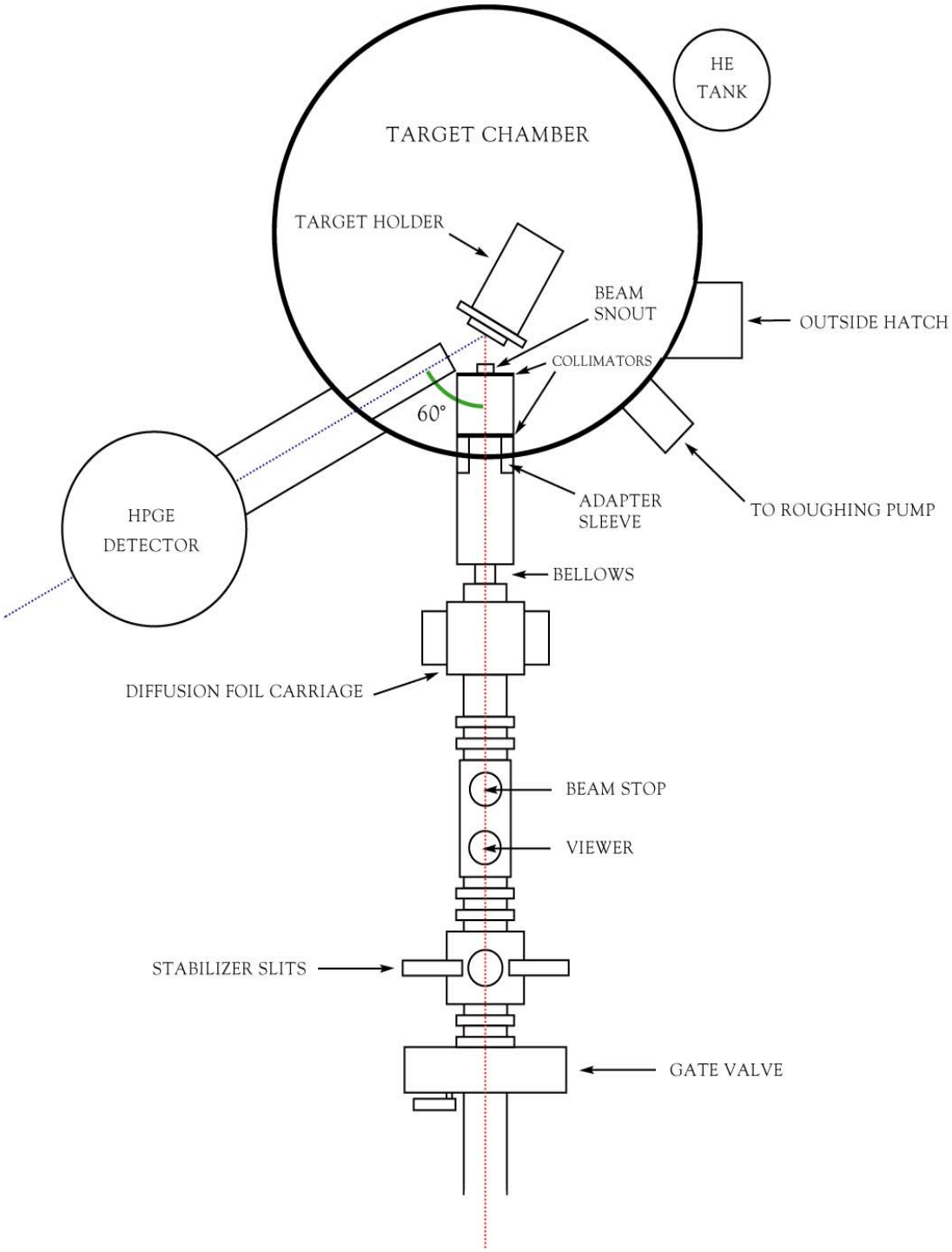

Figure 5: Brigham Young University external-beam line and target chamber, not to scale

could contain a helium atmosphere for the external beam, and with some slight modifications, the chamber could still be used for RBS or standard PIXE. The viewers and diffusion foil carriage from the existing external-beam line were left between the magnet and the chamber. The original beam snout, however, had to be removed from the end of the beamline. A sleeve was machined to fit inside the target chamber's beamline coupling. The snout was shortened and mounted on the end of this sleeve. A pair of O-rings between the sleeve and the coupling allowed the beamline to be evacuated to the Kapton foil at the end of the beam snout, while the target chamber remained at atmospheric pressure.

The target chamber itself required a few modifications to make it usable. A means of attaching a vacuum pump had to be devised, and the open orifices had to be closed. The latter was done by machining a simple plug to hold an O-ring in place over an irregular-sized opening. A copper pipe underneath the chamber was fitted with a brass piece to attach it to a hose from a roughing pump (see Figure 6). The same pipe also

Figure 6: Photograph of copper pipe and helium intake spigot

contained a valve which could be used to open the chamber to the pump. A second tube in this fixture also contained a valve, through which the helium tank was coupled with the chamber. This provided a convenient way to evacuate the chamber and then fill it with helium.

We chose the same geometry as had been previously used in external-beam PIXE experiments at Brigham Young University. This consisted of the axis of the beamline and the axis of the detector forming a 60-degree angle, which was bisected by the normal of the sample (see Figure 7). This geometry allows the beam trajectory and the axis of the detector to be as close as possible to perpendicular to the face of the sample,

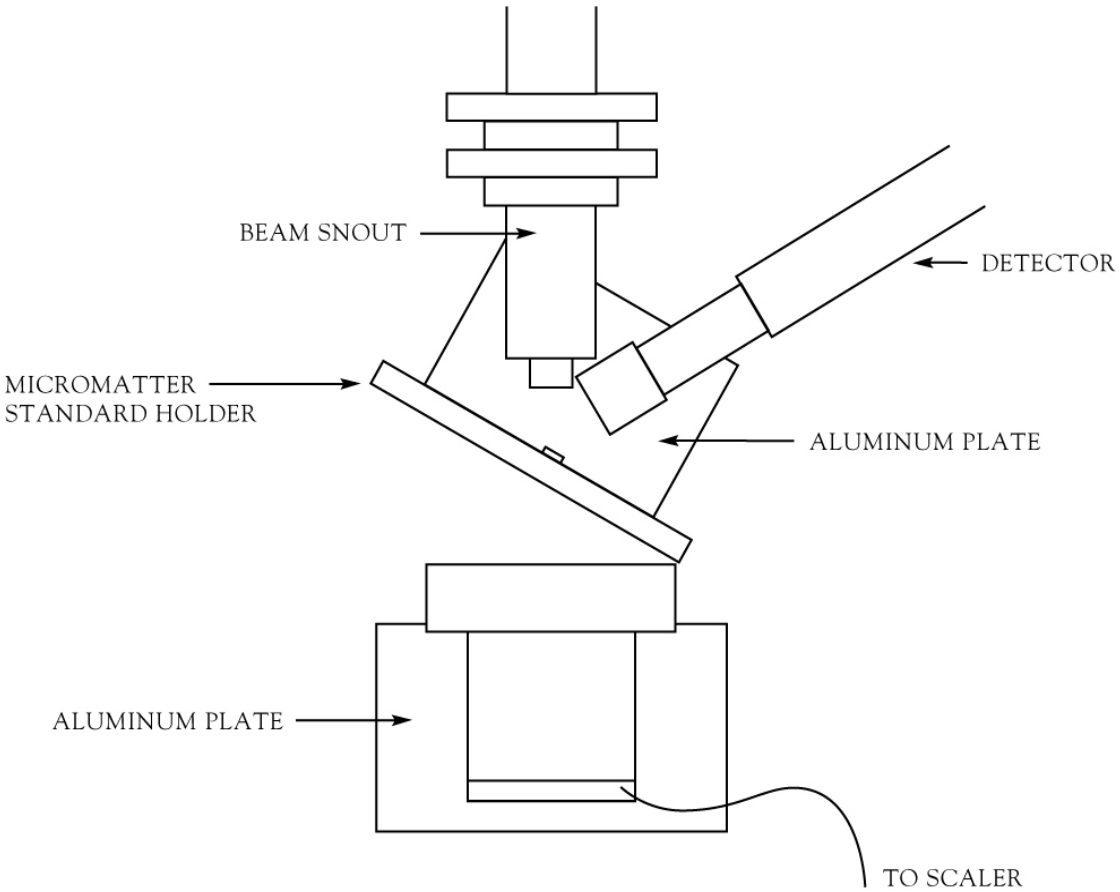

Figure 7: Diagram of target chamber setup for micromatter standard analysis

while minimizing the distances from the beam snout and the detector to the sample. Having the detector close and parallel to the face of the sample is desirable to maximize the solid angle subtended by the detector, thereby also maximizing the amount of radiation that enters it. Minimizing the distance between the beam snout and the sample reduces losses in beam energy and current. If the beam snout and detector were to be moved closer to the sample than we positioned them, the angle between them would have to be further spread, whereas if the angle were to be reduced below 60 degrees, the snouts would have to be retracted. Thus the 60-degree backangle seemed the best compromise to accommodate both a good solid angle and close proximity for the beam and detector.

In order to fix the detector in the correct alignment, we had a fitting made to couple the

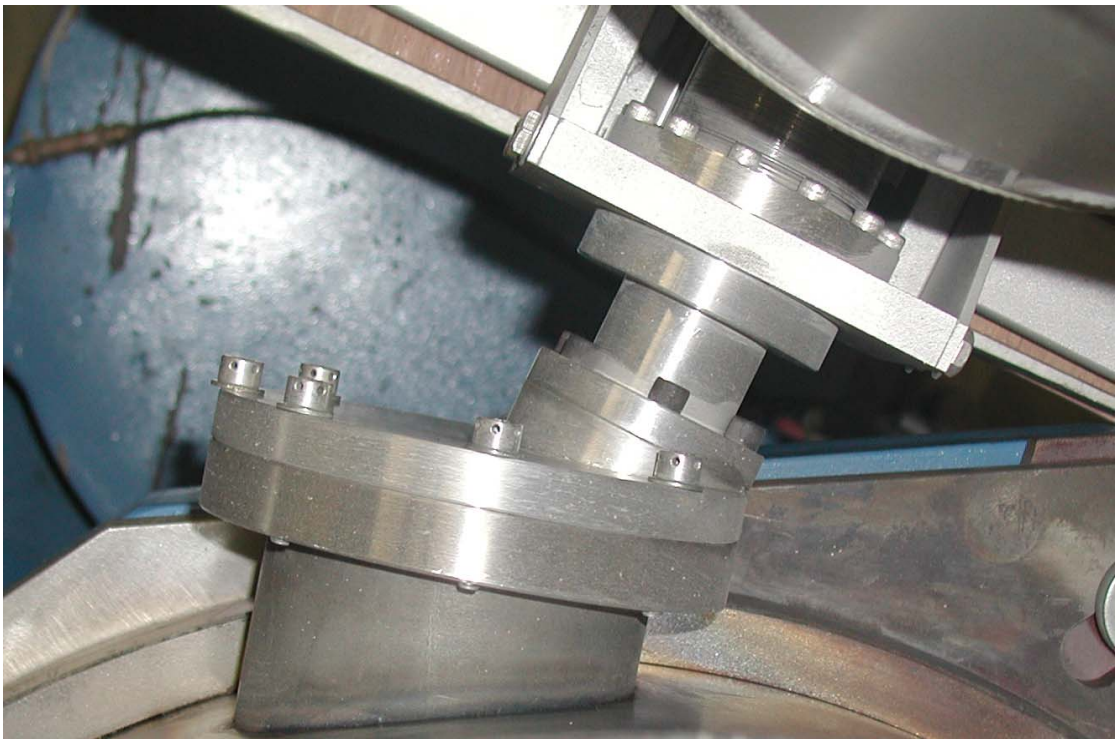

Figure 8: Detector to chamber coupling, top view

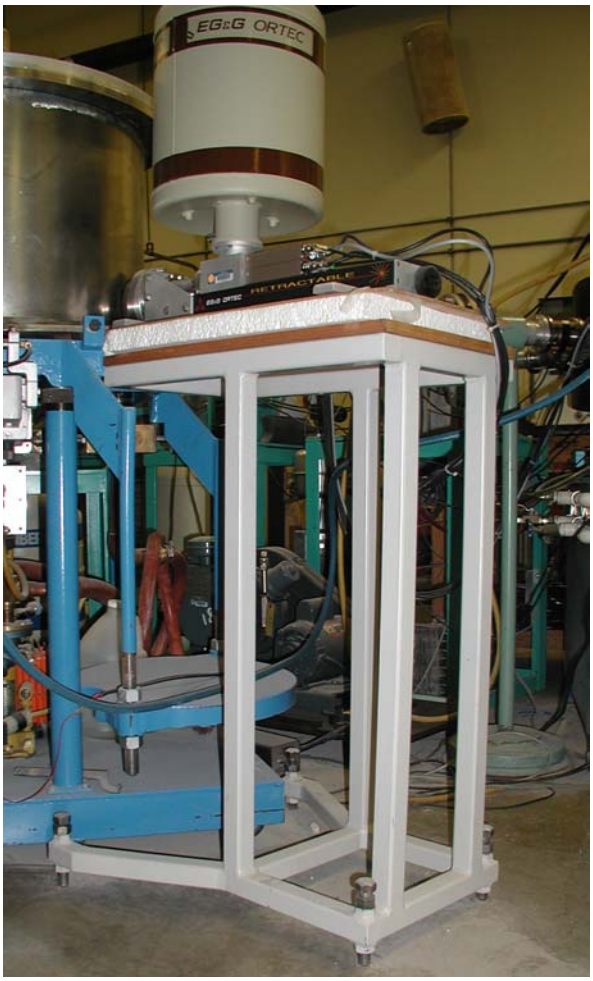

Figure 9: X-ray detector atop detector mounting table

detector case and the target chamber (see Figure 8). A special platform had to be constructed to support the detector when it was bolted into the coupling (see Figure 9). Its feet were made adjustable so that the top could be made level, regardless of the unevenness of the lab floor. These two parts proved to be ideal for mounting the detector in the correct position and alignment. The detector was extended until it was as close to the sample as it could be without interfering with the beam path. The distance it was extended was noted, to allow for easy reproducibility if it should ever have to be retracted. The intersection of the axes of the two snouts was marked as the location of the sample. The edge of an aluminum plate was mounted on the target chamber floor to coincide with the intended orientation of the sample at this point. A mark was made on the plate to show where the collimated, centered beam should strike the target, so that it could be centered properly.

Two types of samples were to be accommodated in the new setup. The first were thin targets: micromatter standards. These were used in the calibration of the detector and analysis software. The second were coins, which had to be supported differently because of their thickness. The micromatter standard foils were mounted in thin aluminum target frames, which fit the dimensions of the target holder in the south beamline. The frames also provided a convenient way to mount them in the external beam system. A screw was used to hold them flat against a thin piece of wood with a hole drilled through it. The hole coincided with the part of the frame that contain the micromatter foil. This allowed the beam to pass through the foil and the holder to a Faraday cup behind both (see Figure 7). The Faraday cup collected whatever protons passed through the foil to give an integrated charge measurement.

Coins must be mounted differently because they are not already fitted into frames, they have different diameters and thicknesses, and they stop the beam current, making a Faraday cup useless. With the help of the expert machinist Wes Lifferth, we designed a target holder that would allow us to accommodate all of these conditions (see Figure 10). To use it, coins are first measured for thickness, then mounted on a detachable target holder with Teflon clamps. The Teflon does not scratch the surface of the metals, making them well-suited to handling valuable samples. The target holder is made of aluminum, which will also not scratch a coin if it is handled carefully. The coin is positioned precisely with respect to where the beam will strike through use of a cross-hair that is etched into the surface of the target holder. The clamps are then angled to accommodate a coin of any size between 0.375 and 1.5 inches diameter (see Figure 11).

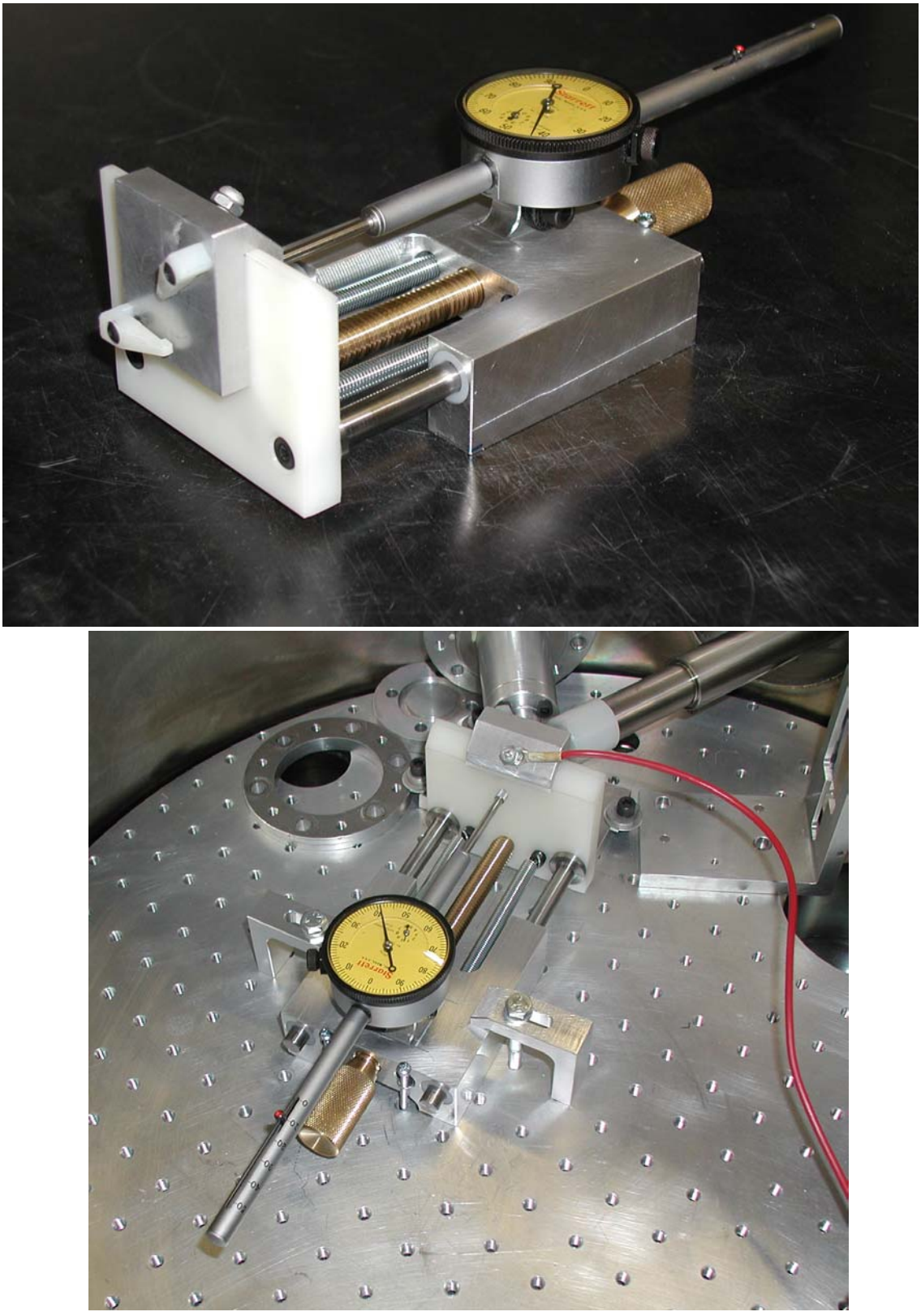

Figure 10: Target holder, glamour shot (top) and in full implementation (bottom)

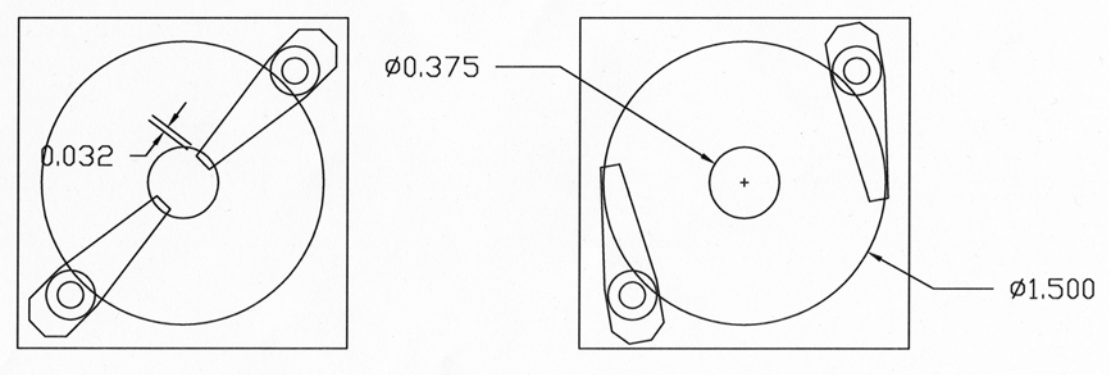

Figure 11: Target holder mechanism for securing coins of any diameter between 3/8" and 1.5"

The tightness of the clamps can be adjusted to secure coins from 0.03125 to 0.25 inches thick. Once the coin is mounted, the holder is placed on a larger frame that is adjustable in the direction of the normal of the sample. The position is adjusted to account for the thickness of the coin, causing the face of the coin to coincide with the proper plane. A micrometer allows for a careful adjustment of the position, to the nearest .01 mm. Finally, a wire lead is attached to the top of the target holder and connected to the scaler. Since the coin and the target holder are conductors, the sample acts as its own Faraday cup, and the beam current is transferred without any post-target loss to the scaler. Thus, the target holder secures coins of nearly any thickness, positions them correctly, and acts as a Faraday cup. This device greatly expedites the process of changing and aligning samples, which is important to preserving the purity of the helium atmosphere in the target chamber.

Our last step in preparing the external-beam equipment was to set up the detector and the supporting electronics. A new data acquisition bin was assembled and configured to accompany the new detector. The bin was connected to the desktop computer through a coaxial network connection. We installed and configured Canberra's Genie software to

interface with the detector electronics for spectrum collection (Canberra Industries, Meriden, CT). Once this was accomplished, testing began to determine the optimal settings in the hardware and software for energy resolution in our spectra. We found that even with the best possible settings, the resolution still was not as good as it should have been, based on our work with the south beamline. We also found that we had a very high low-energy background. We placed a beryllium window in front of the detector to attempt to filter stray protons that might find their way into the detector. This helped our problems minimally. We then added a layer of mylar, which dramatically reduced the number of low-energy X rays reaching the detector. The lower background and reduced low-energy count rate greatly helped our detector dead time. It appeared that this improved our energy resolution, though not to the extent that we had hoped. We determined that the improvement in the background level was adequate for our purposes, so we chose to operate with both filters in place.

Once we had obtained some calibration spectra, we characterized the detector in GUPIX. The characterization allowed us to adjust parameters in the software to assist it in fitting the spectra from the detector. After several attempts, we felt we had a close enough similarity between the parameters in the model and the actual properties of the detector.

At one point, the computer we used to collect spectra had to be completely reconfigured due to software changes on the department network. This was a very good exercise in setting everything up again, and after about two months, all was working as well as, or

even better than, before. One of the greatest challenges of this process was reinstalling the code which allowed us to convert Genie Camfiles into a GUPIX-readable file format.

Constructing, testing, and refining our equipment comprised a considerable amount of time. As one piece of equipment was completed, the need for another piece became apparent to use our gear to the greatest effectiveness. Once all of the parts were assembled, we determined that our apparatus afforded us a great deal of ease in performing the kind of quality analysis we were striving for. However, with beam time being sometimes difficult to obtain and of unpredictable duration, we did not wait until every phase of construction was complete before we began calibration. The target holder, the crowning piece of equipment for our apparatus, was not finished until long after the detector calibration had been completed. Nevertheless, the effort we put into designing our machinery paid great dividends in allowing us to work quickly, without wasting precious beam time to rerun samples. The equipment will be useful in many sorts of future studies at Brigham Young University.

CHAPTER III

METHODS

Once all of the equipment was assembled, the next step consisted of a careful calibration of the detection and analysis systems. This was a two-step procedure, beginning with the analysis of micromatter standards followed by thick-target standards.

Micromatter standards are thin mylar foils with an element or compound deposited on one side. The concentration of each element on the foil is known with moderate certainty (within five percent) so that the standard can be used as a means of calibrating the x-ray detector.[13] Several of these standards were selected to provide a representation of the entire spectrum in our analysis. In terms of elements with observable K lines, these ranged from titanium to tin. In terms of energy, this ranged from about 4 to 25 keV. Many elements with L lines in this energy range were also selected.

With the accelerator set to the lowest energy that would produce any spectrum from the manganese standard, we calculated a beam energy in the beamline of 1.002 MeV. In making this calculation, we compared the field strength of the steering magnet for the low-energy beam to the standard high-energy beam, which we knew to be 2.100 MeV.

This is the energy necessary to direct the beam into the south beamline at a particular magnet setting. Through the ratio of the squares of the field strengths, we found the particle energy as it passed through the magnet to be 1.002 MeV.

$$B^2 \propto KE$$

$$\frac{B_1^2}{B_2^2} = \frac{KE_1}{KE_2}$$

$$\frac{319.1^2}{462.0^2} = \frac{KE_1}{2.1}$$

$$KE_1 = 1.002$$

We chose to experiment initially with three energies: 1.002 MeV, 1.499 MeV, and 2.100 MeV. The middle energy corresponds to a fairly stable region about halfway between the lowest and highest energies. We found that at the lowest energy, we could not read a beam current in our Faraday cup. Without an integrated charge, it is difficult to determine absolute concentrations in the sample. Therefore, we retained for our calibration at the lowest energy only the samples with two elements in the detectable energy range. Even though we could not determine absolute concentrations in these targets, we could at least find the relative concentration of the two elements.

In order to analyze the samples, a plate was fixed to the floor of the target chamber, with one edge at the appropriate angle and distance for the location of a target. The micromatter target was attached to a wooden stand with a hole drilled to expose the sample on the back side, allowing the beam to pass through. The stand was placed flush

with the plate in such a manner that the micromatter foil was aligned with the beam snout. Finally, a Faraday cup was placed behind the target to collect the beam current after it passed through the target (see Figure 7).

Each micromatter standard was run until about 1.5 microcoulombs of integrated charge was collected at the Faraday cup. In the case of the 1.002 MeV runs, the duration of sampling was more arbitrary, though peak height and definition in the sample elements were commonly the standards for determining when enough data had been collected.

Because it was much easier to change targets than beam energy, all samples were run at one setting before adjusting the accelerator to a different energy. The use of helium atmosphere in the target chamber necessitated a meticulous procedure to maintain the same conditions from one target to the next. At the beginning of the session, while the accelerator was coming up to pressure, we pumped the target chamber out with a roughing pump, down to approximately 10^{-3} Torr. Then the valves to the helium tank were opened to purge the helium lines. The pump valve was shut and helium was allowed to flow into the chamber until the pressure on the chamber door was released. When a target was to be changed, helium flow was turned on before opening the hatch. The chamber was then briefly opened for the operator to reach inside and remove the sample. The hatch was then closed again while the target on the holder was changed. The target was replaced, the hatch resealed, and the helium flow turned off. This method seemed to provide a good compromise between convenience and care in handling the samples. Though some mixing of air with the tank gasses was permitted

using this method, no observable increase in background levels or even argon peak levels could be seen throughout the day.

After a spectrum had been obtained for a standard, it was analyzed with GUPIX to determine the elemental concentrations. This yielded a concentration for each element in terms of micrograms/cm^2. An H-value for the element could then be obtained by dividing this concentration into the product of the integrated charge (in microcoulombs) and the areal density of the sample (in micrograms/cm^2). H-values are correction factors that make observed concentrations in samples more similar to their actual values. Although GUPIX considers many factors that influence the x-ray yield from the sample, including the geometry of the experimental setup, the type of x-ray detector, and the beam energy, not every detail can be accounted for and some discrepancy persists. The H-values correct for these systematic sources of error that are consistent from one sample to another, therefore they improve the accuracy of absolute concentration values without adversely affecting the comparability of different spectra. When several standards had been analyzed, a plot of H-values versus emission energy could be made. We generated such a plot, as will be described later.

Another important factor to the quality of the GUPIX analysis was the accuracy of our estimate of the beam energy when it reached the target. The beam energies listed above apply as the beam passes through the evacuated beamline and are based on accelerator column current measurements and field strengths in the steering magnet. However, by the time the beam actually reaches the sample, it has traveled through the carbon

diffusion foil, the Kapton window, and about two centimeters of a helium-air mixture. Each of these cause the beam to lose energy, so the energy on target is considerably lower than the beam energy in vacuum.

Originally, we planned to use the energy values obtained through the Matlab code as a starting point for an iterative procedure involving GUPIX and H-values. We reasoned that by using our adjusted energy as the beam energy in a GUPIX analysis, we would obtain a set of H-values. These H-values could then be applied to a target of known composition, such as the silver-copper dime. First we ran GUPIX on the copper and silver micromatter standards with an initial beam energy that was our best estimate, according to the Matlab routine. From this fit, we obtained H-values for these two elements, which we then applied to our analysis of the dime. Keeping the H-values constant, we varied the energy of the beam in GUPIX until the dime analysis yielded a 9:1 silver to copper ratio. The energy needed to achieve the correct ratio was then put back into GUPIX as the beam energy for the micromatter standards, and the analysis was repeated. It was our hope that through this process, we would arrive at the correct beam energies and H-values simultaneously, as the beam energy converged to the actual value. This was not the case, however, as very slight changes in H-values could lead to large changes in the calculated beam energy. We abandoned this approach in favor of a simpler one.

Knowing that the on-target beam energy at the lowest setting had to be close to zero, we set about trying to find a Kapton thickness that would reduce the beam at this energy to

nearly zero. The Kapton was the least-known thickness of consequence in the beam path. Therefore we sought to apply inductive reasoning to determine its actual thickness, or at least an effective thickness that would agree with the beam's exhibited behavior. Since we had determined 1.002 MeV to be the initial energy of the lowest setting, we used this value as the starting point for the Matlab routine, through which we varied the thickness of the Kapton until an on-target energy of 15.1 keV was obtained. The density we eventually used was 8.52 g/m^2. According to Dupont, the tolerances for this thickness of Kapton are 7.6-14.0 g/m^2.[14] Since our calculated value fit into the accepted range of areal densities from the manufacturer, we decided to use this as the actual thickness of the Kapton. The on-target values of the other two beam energies were then calculated to be 1.701 MeV and 953 keV. We computed the range for protons at these two energies in a few metals of interest (see Table 1). These ranges correspond to the approximate stopping depth of the beam, and therefore the maximum depth at which characteristic X rays could be produced.

Using these energies, we put all of the micromatter standards' spectra through GUPIX and generated a set of H-values for the highest two energies. The lowest energy was below the 200-keV minimum for GUPIX, so we ceased to analyze this level. In comparing the H-values for the upper two energies, we found that the sets exhibited similarities in many regards, including the relative placement of K- versus L-

Table 1: Proton ranges (in microns) in metals at our selected beam energies

Beam energy	Au	Ag	Cu
1701 keV	13.03	15.57	14.79
953 keV	5.97	6.74	6.61

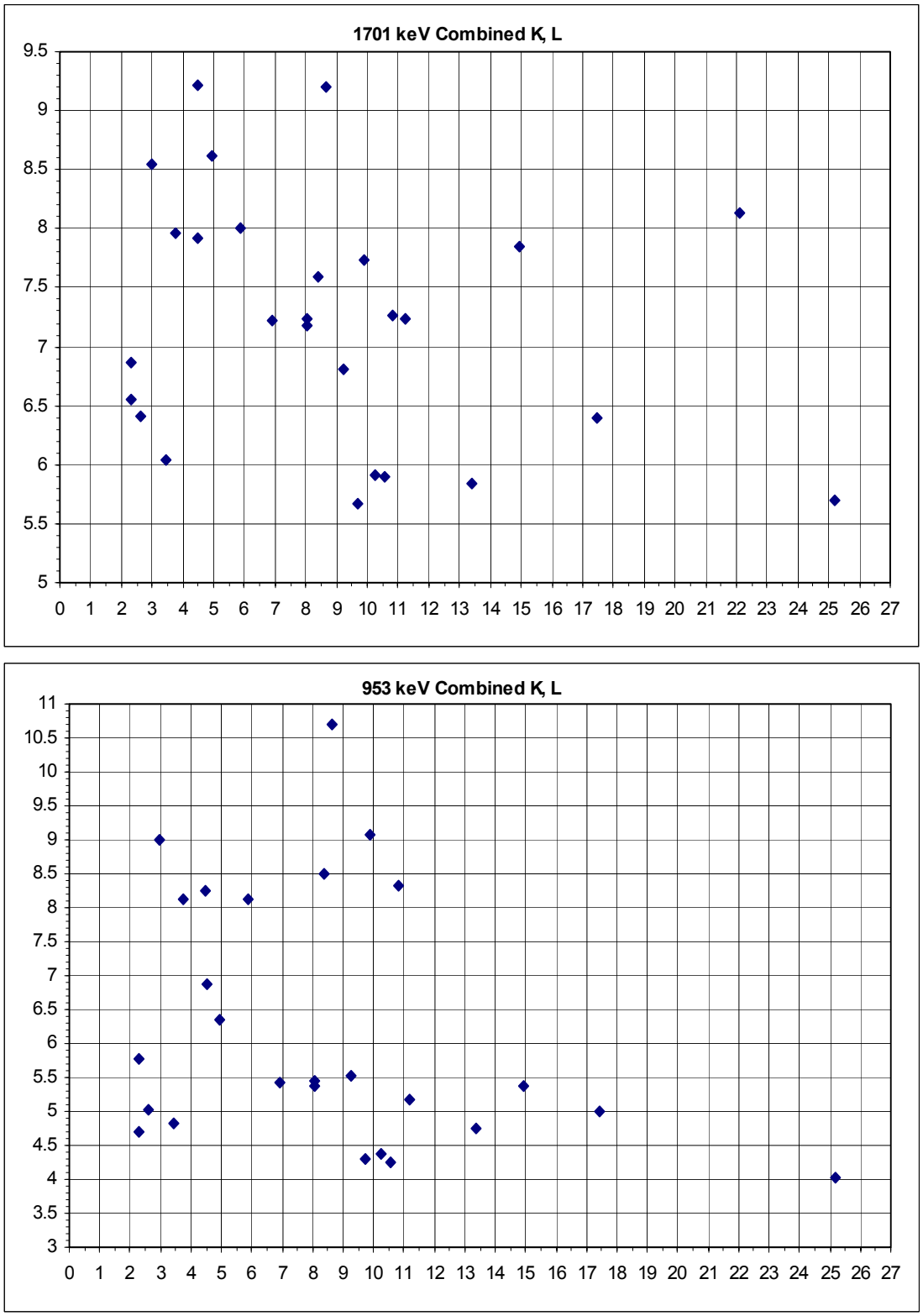

Figure 12: H-value plots for K and L lines as a function of x-ray energy at both beam energies

emission H-values and the general trend in the magnitude of H-values as a function of emission energy (see Figure 12). In both cases, the L-emission values fell below the K values of similar energy. The general trend at both energies was to have high H-values for low-energy emission lines, which then decreased and leveled off as energy increased. The H-values for the 953-keV sequence averaged about three-fourths of their higher-energy counterparts.

Encouraged by these similarities, we drew curves through what could believably be called the averages of the two sets of H-values. We attempted to remain near the calculated values for copper, since this element will be found in most of our samples. Unfortunately, the silver H-values appeared to be definite outliers. Uncertainties about the present concentrations of the silver micromatter foil may account for this error. At high energy, we instead followed the tin and molybdenum K-lines. We did not extrapolate the curves below 4 keV on the low end.

The curves seem to agree with the basic characteristics we expected to find in the H-values. The lower-energy emissions are counted less efficiently than the higher energy ones, and therefore have higher H-values. As energy increases, the H-values decrease smoothly and level out where the counting efficiency stabilizes. The actual shape of the graph may be rather subjective, but preliminary examinations have shown that in regions of greatest interest, or at least around copper and silver, the H-values give believable relative concentrations and are therefore valid. Perhaps this is in part due to the fact that we chose to follow copper in the way the curve is pitched in that region of

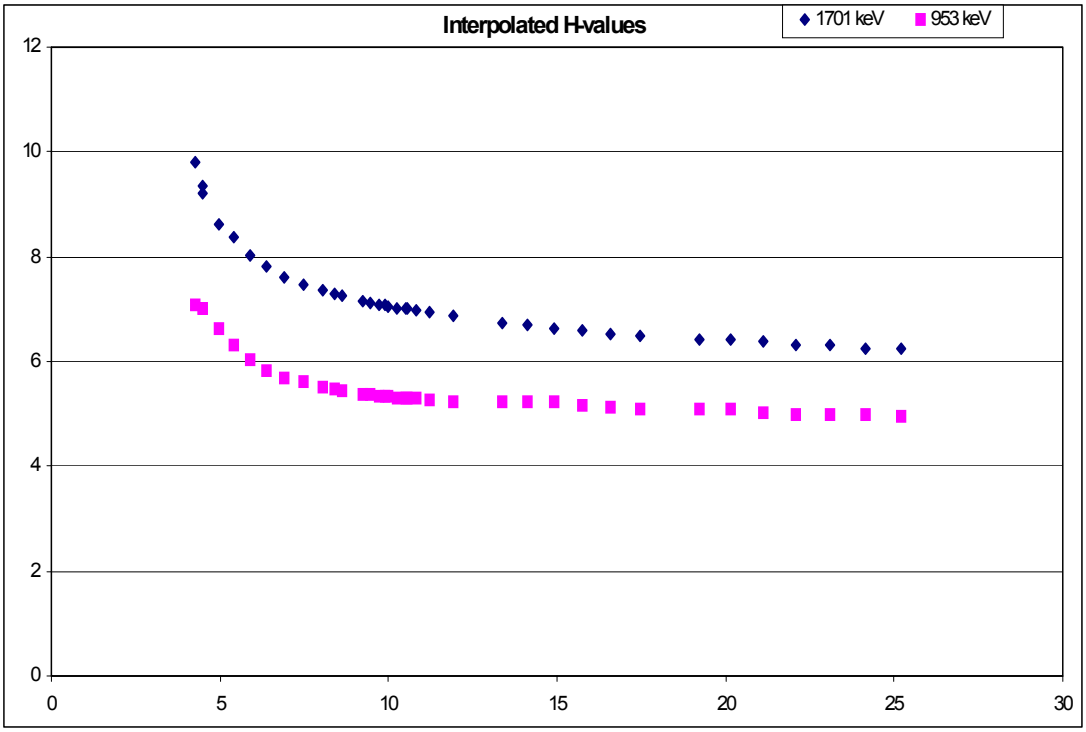

Figure 13: Interpolated H-value curves as a function of x-ray energy for both beam energies

uncertain curvature. Nevertheless, as the H-values do not generally need to be very exact, the model we have generated seems to work for our purposes so far.

From these curves we interpolated a new set of H-values for the two energies by locating the value on the graph corresponding to the energy of the desired emission line (see Figure 13). These are the H-values we used in calculating the concentrations in our samples.

In order to further improve our results, we might suggest making a few changes to our procedure. First, a better measurement of the integrated charge could be obtained if the Faraday cup were positioned closer to the sample. In fact, it would be worth trying to

mount the micromatter standards on the target holder used for thick targets. Since the target holder is a conductor, virtually all protons that pass through the foil would then be counted in the integrated charge measurement. Of course, the aluminum peak would have to be subtracted from the spectrum, but with the filters we have on the detector, very little aluminum is actually detected in our spectra. Also, when the experiment was performed, I was not aware that the micromatter standards have a "front" and "back" with respect to where the standard elements are deposited. It is possible that some targets were run from the back, thus further decreasing the beam energy before they actually interacted with the elements of interest. Finally, in some cases, the exact stoichiometry of the samples was unknown. Even in the best cases, the concentrations given are only certified to about five percent.[13] This could be improved by the creation of a customized set of thick-target standards. In this way, the concentrations could be verified by a number of methods and the elements of greatest interest to our studies could be emphasized. It would furthermore be more consistent with our sample types to use thick standards, rather than extrapolating the results of thin targets to our work.

CHAPTER IV

SAMPLES AND RESULTS

After satisfactorily calibrating the system, we turned our attention to experimenting on a number of samples. We selected several modern coins with the intent of using them mostly as standards. We also analyzed five ancient bronzes, since we had previous experience in examining bronze. We found it very interesting that during the course of the analysis, the modern "standards" became a more significant sample set than the bronzes.

Our modern coins were selected as standards because their initial composition was known to a high degree of accuracy, thanks to the care invested by the US Treasury Department. These included a 1963 dime with a 90%-10% silver-copper composition which we used as our primary standard. This was the dime used in the H-value and beam energy calibrations. We also used a 1965 Kennedy half-dollar, which had an 80%-20% silver to copper composition in the outer cladding. An unstruck 25-cent piece, or planchet, provided a standard with a clean surface (abbreviated BLNK). Finally, a 1915 Mexican gold two-Peso coin was used for comparison to the silver-copper compounds because of the nobility of gold atoms. Later in the procedure, we milled half of the face off of a 1928 "walking liberty" half dollar. This was done to compare the composition at the surface to the center of the coin. Unfortunately, this

sample was never examined with the external beam, though it was subjected to other methods.

The following ancient coins were examined:

Egypt Ptolemy IV (222-204 BC), Zeus and eagle on thunderbolt (abbreviated EGPT)

Augustus (27 BC-14 AD), bare head right (abbreviated AUGU)

Trajan (98-117 AD), laureate head right (abbreviated TRAJ)

Egypt Ptolemy II (285-246 BC), Alexander w/elephant skin headdress (PTO2)

Seleucid Empire Antiochus VIII Philometor (145-142 BC), radiating head (SELE)

Little is known of the provenance of these coins, but we anticipated that at some point in the last 2000 years, they would have been subjected to environmental conditions that would promote surface enrichment. All showed obvious signs of wear and corrosion. In order to better examine the alloy composition, they were mounted so that the proton beam would strike them on a relatively smooth area.

The Appendix contains tables of the values obtained for each coin at the two energies of our analysis. All of the coins contain elements we expected to see in them. The ancient coins are composed largely of copper, tin, lead, and trace elements, including iron. TRAJ and AUGU are comprised almost solely of copper, while the rest are more traditional old-world bronzes. The modern coins also have concentrations near their expected values.

Below is a table showing the copper concentration for each coin at both beam energies (see Table 2). By comparing the concentrations at the two energies one coin at a time, we can assess the effectiveness of this depth profiling method in finding surface enrichment. In each of the modern coins except the planchet, the copper concentration decreases significantly while the silver fraction increases (or gold fraction, in the two-Peso piece). However, in each of the ancient coins, the concentration of copper hardly changes or the change is not statistically significant. The error values in the table were determined using the fit error reported by GUPIX. Other sources of error were not easily quantifiable, and will be discussed later. Nevertheless, the errors arising from the GUPIX fit provide an adequate reference for comparing the concentrations from the two energies. Since copper is more reactive than silver or gold, a depletion in copper at the surface suggests that copper has been removed by chemicals in the environment. It therefore appears that our multienergetic PIXE has detected surface enrichment in the modern samples.

Table 2: PIXE copper concentrations at both energies

Modern Coins	**% Cu at 1701 keV**	**% Cu at 953 keV**	**Expected value**
Dime	9.098±0.022	7.067±0.053	10
Half	16.398±0.036	11.761±0.068	20
Blnk	74.165±0.142	74.586±0.075	75
Peso	9.318±0.018	8.800±0.021	10

Ancient Coins	**% Cu at 1701 keV**	**% Cu at 953 keV**
Egpt	64.134±0.149	63.799±0.383
Augu	99.285±0.075	98.288±0.638
Traj	98.683±0.210	98.670±0.077
Pto2	81.474±0.207	80.113±0.969
Sele	65.851±0.289	65.632±1.215

Because only modern samples exhibited significant differences between the two beam energies, it appears they are more suited to surface enrichment studies with the equipment we have. The depth to which the proton beam can penetrate is limited by the maximum beam energy of the accelerator. It is possible that the ancient coins underwent surface enrichment centuries ago, and in order to find an appreciable difference between the surface and the inner parts of the coin, a much higher-energy beam is needed. If this is so, then the modern coins may be in a period in which their surface enrichment has just begun and can be observed with the Brigham Young University accelerator.

Other methods were employed to attempt to corroborate our PIXE data. These include XRF, which penetrates much more deeply than PIXE, and scanning electron microscopy (SEM), which scans only the surface layers of atoms. In several cases, the same coins used in PIXE were subjected to these methods. The other methods agreed

Table 3: Copper concentration by coin comparing PIXE, XRF, and SEM

Coin	XRF	PIXE 1701 keV	PIXE 953 keV	SEM
Dime	9.24±0.23	9.098±0.022	7.067±0.053	5.30±0.24
Peso	N/A	9.318±0.018	8.800±0.021	8.37±0.20
Blnk	N/A	74.165±0.142	74.586±0.075	74.63±0.22
Sele	N/A	65.851±0.289	65.632±1.215	60.96±1.04
Egpt	N/A	64.134±0.149	63.799±0.383	63.15±0.21
Traj	N/A	98.683±0.210	98.670±0.077	96.74±0.31
Augu	N/A	99.285±0.075	98.288±0.638	96.26±0.36
Pto2	N/A	81.474±0.207	80.113±0.969	81.37±0.41

with the PIXE results, suggesting that the concentration changes we observed with PIXE fit into a greater trend of surface enrichment (see Table 3). XRF and SEM studies done with other coins support the data, though they are not included here because they are not as directly applicable to the PIXE study. However, the calibration of the XRF and SEM data seems correct, so it can be compared to the PIXE data.

Of the sources of possible error in this study, the uncertainty in the H-values is the most significant. The H-values enter the concentration and error calculations after GUPIX has computed its results, and therefore offer a final opportunity for error to enter as the results are calculated. Normally the arbitrariness of the H-value curves is not especially significant when the same curve is used to compare many samples and the curve is reasonably close to the actual values. However, in this study, we compare the values generated by two different sets of H-values, so if one curve is drawn too high or low, it impacts the ability to compare the two. We believe that the data obtained through other methods and the consistency of the results within our data set show that our H-value curves are reasonably well calibrated. Improving our confidence in these values would greatly enhance our ability to study the surface enrichment effect, particularly if we were to analyze at several more energies in the range of our accelerator's capability.

Additionally, we noted that the fit errors for the ancient coins are generally higher than those of the modern coins. This can be explained by the presence of many more trace elements in the ancient coins. The tails from the peaks of these elements have the effect of raising the background level, so the signal to noise ratio is adversely affected. The

increase in the number of elements also adds variables to the fit, which prevents GUPIX from fitting each one as precisely. Nevertheless, even if the error in the percent composition of the ancient coins were improved, the normalized values would still be much closer from energy to energy than those of the modern coins, and our conclusions would be the same.

CHAPTER V

CONCLUSIONS

In consequence of our research, we have demonstrated that we can observe statistically different compositions with different beam energies in modern coins. We believe that a more powerful accelerator would allow us to peer farther into the interior of ancient coins and perhaps observe the same effect in them as well. We believe our observations in modern coins are the result of the surface enrichment effect, as the more reactive metals are present in lower concentrations at the surface. We also have a feel for the error in concentration of major elements. For modern coins whose alloy constituents are not close on the periodic table, this appears to be about .02%. For ancient coins, the error is quite a bit higher because of the presence of so many more elements in greater concentration, so it is not possible to generalize.

One possible application of our research is in coin authentication. Since we have observed surface enrichment close to the surface of modern coins, it may be used as a distinguishing feature of a recently minted sample. Thus depth profiling may be able to detect a modern counterfeit of an ancient coin, though ancient counterfeits and counterfeits of modern coins could not be detected on this basis alone. In order for this process to be confidently implemented, more research would need to be done to

determine whether artificial aging techniques are limited to the surface or penetrate deep into the bulk of the coin, making a PIXE depth profile inconclusive.

Several aspects of this research could be improved with additional time and more advanced equipment. A more energetic beam would allow us to analyze at a greater depth and expand the range over which we could sample. This would improve the credibility of our results by allowing us to analyze at more energy settings. Even with our present equipment, we suggest adding more calibrated energies to our toolkit. Now that we have a greater familiarity with the beam energy, we could more accurately add a low energy below 953 keV, as well as several between 953 and 1701 keV. When the time comes to replace the Kapton foil again, I would recommend measuring the areal density of the new window to verify how well it agrees with the calculations we did during this experiment. This would help us specify our beam energy and give us a slight improvement in the GUPIX analysis. If it were possible to improve the energy resolution of the detector, that would help reduce the statistical error in our spectra. Improving the counting efficiency of the detector would also aid in this regard. Finally, a more accurate calibration would greatly benefit our confidence. Concentrations obtained from different beam energies could be more properly compared if the Faraday cup were directly behind the micromatter standards or if thick, conducting standards were used. In this way, less beam current would be lost at lower energies as protons travel to the Faraday cup, and the H-value curves could be placed more exactly. By taking these steps in a future calibration, we could reduce the error introduced by H-

values and make a better assertion of how the composition changes as a function of depth.

Through our study in PIXE depth profiling, we believe that PIXE would play an important role in a multifaceted analysis using XRF, SEM, and PIXE. Regions of interest in the coin are accessible with PIXE, particularly in modern samples. The beam energy in PIXE can also be varied with relative ease, allowing for a more detailed depth profile. With our PIXE data corroborated by XRF and SEM on either side, we will be able to offer coin collectors a highly accurate, nondestructive means of finding coin composition over a broad range of depths.

APPENDIX

The tables in this appendix represent data collected on the coin specified on the top of the page. In order to conserve space at the head of each column, I have abbreviated the headings. This page will explain in greater detail what the ambiguous titles represent.

Column 3: Concentration—concentration as reported by GUPIX, in arbitrary units because the calibration does not allow the computation of absolute concentrations

Column 4: % Error—fit error as reported by GUPIX

Column 5: Adjusted Concentration—concentration value reported in column 3, multiplied by the H-value

Column 6: Adjusted Error—adjusted concentration value reported in column 5, multiplied by the error reported in column 4—converts error from a percentage to a range in arbitrary units of concentration

Column 7: Normalized %—concentration now converted to the atomic fraction of that element in the sample—note that these numbers are percentages

Column 8: Error in %—error in the normalized concentration, in terms of percent concentration—represents the "±" value of the normalized percentage

DIME

1701 keV

Element	H-value	Concentration	% Error	Adjusted Concentration	Adjusted Error	Normalized %	Error in %
Ti	9.21	10.9	7.64	100.389	7.6697196	0.009203956	0.00070332
Cr	8.38	30.6	2.55	256.428	6.538914	0.023510065	0.0006009
Fe	7.81	99.2	0.93	774.752	7.2051936	0.071031517	0.0006727
Ni	7.45	53.9	1.63	401.555	6.5453465	0.03681573	0.00060362
Cu	7.35	13501	0.17	99232.35	168.694995	9.09791049	0.02169649
Zn	7.25	7.7	126.82	55.825	70.797265	0.005118198	0.00649057
Ag Ka	6.33	156363.4	0.2	989780.322	1979.560644	90.74593894	0.0228393
HgL	7.05	16.2	26.85	114.21	30.665385	0.010471105	0.00281126

953 keV

Element	H-value	Concentration	% Error	Adjusted Concentration	Adjusted Error	Normalized %	Error in %
Ti	7	19	11.52	133	15.3216	0.008966589	0.0010345
Cr	6.3	44.6	4.15	280.98	11.66067	0.0189431	0.00079557
Fe	5.83	195.5	1.5	1139.765	17.096475	0.076840637	0.00125533
Ni	5.6	125.1	2.54	700.56	17.794224	0.047230329	0.00123775
Cu	5.5	19058.7	0.39	104822.85	408.809115	7.0669432	0.0525513
Zn	5.43	42.2	44.12	229.146	101.0992152	0.015448557	0.00681559
Ag Ka	5	275152	0.7	1375760	9630.32	92.7509391	0.05417093
HgL	5.34	40.8	34.51	217.872	75.1876272	0.014688487	0.00506915

BLNK

1701 keV

Element	H-value	Concentration	% Error	Adjusted Concentration	Adjusted Error	Normalized %	Error in %
Cr	8.38	2	11.67	16.76	1.955892	0.004415102	0.000515508
Mn	8.02	175.8	0.65	1409.916	9.164454	0.371415424	0.002808611
Fe	7.81	34	1.95	265.54	5.17803	0.069951438	0.001390195
Ni	7.45	12888.1	0.5	96016.345	480.081725	25.29367104	0.132880911
Cu Ka	7.35	38304.2	0.49	281535.87	1379.525763	74.16524428	0.141541038
Zn	7.25	49.9	69.56	361.775	251.65069	0.09530271	0.066230401

953 keV

Element	H-value	Concentration	% Error	Adjusted Concentration	Adjusted Error	Normalized %	Error in %
Cr	6.3	4.5	20.57	28.35	5.831595	0.003958227	0.000814208
Mn	6.04	419.1	0.8	2531.364	20.250912	0.353429057	0.002891355
Fe	5.83	91.1	2.97	531.113	15.7740561	0.074154	0.002204957
Ni	5.6	31782	0.24	177979.2	427.15008	24.849457	0.062254066
Cu	5.5	97128.4	0.22	534206.2	1175.25364	74.58587293	0.074549138
Zn	5.43	175.6	43.11	953.508	411.0572988	0.133128793	0.057315889

HALF

1701 keV

Element	H-value	Concentration	% Error	Adjusted Concentration	Adjusted Error	Normalized %	Error in %
Fe	7.81	20.5	3.6	160.105	5.76378	0.014527911	0.000523566
Ni	7.45	6.8	13.23	50.66	6.702318	0.004596883	0.000608195
Cu	7.35	24587.4	0.16	180717.39	289.147824	16.39827693	0.036232917
Zn	7.25	9.3	182.23	67.425	122.8685775	0.006118137	0.011148405
Ag Ka	6.33	145506.4	0.21	921055.512	1934.216575	83.57648014	0.03740322

953 keV

Element	H-value	Concentration	% Error	Adjusted Concentration	Adjusted Error	Normalized %	Error in %
Fe	5.83	54.7	5.86	318.901	18.6875986	0.012131562	0.000713452
Ni	5.6	14.2	23.14	79.52	18.400928	0.003025082	0.000700149
Cu	5.5	56210.7	0.32	309158.85	989.30832	11.76095333	0.067836449
Zn	5.43	12.6	365.69	68.418	250.1977842	0.002602743	0.009517731
Ag Ka	5	463812.6	0.57	2319063	13218.6591	88.22128728	0.068424604

PESO

1701 keV								
Element	H-value	Concentration	% Error	Adjusted Concentration	Adjusted Error	Normalized %	Error in %	
Fe	7.81	48.7	1.24	380.347	4.7163028	0.068544476		0.000850916
Ni	7.45	30.8	2.26	229.46	5.185796	0.041352279		0.000934687
Cu	7.35	7034.3	0.2	51702.105	103.40421	9.317527612		0.018197828
Au L3	7.09	70885.6	0.08	502578.904	402.0631232	90.57257563		0.018244068

953 keV								
Element	H-value	Concentration	% Error	Adjusted Concentration	Adjusted Error	Normalized %	Error in %	
Cr	6.3	4.5	34.22	28.35	9.70137	0.001954278		0.000668744
Fe	5.83	148.4	1.6	865.172	13.842752	0.059639728		0.000955621
Ni	5.6	85.2	3.47	477.12	16.556064	0.032889769		0.001141397
Cu	5.5	23209.6	0.24	127652.8	306.36672	8.799612358		0.021184026
Au L3	5.35	247035.6	0.11	1321640.46	1453.804506	91.10590387		0.021257028

EGPT

1701 keV

Element	H-value	Concentration	% Error	Adjusted Concentration	Adjusted Error	Normalized %	Error in %
Mn	8.02	1.2	20.73	9.624	1.9950552	0.003157901	0.000654659
Fe	7.81	228	0.45	1780.68	8.01306	0.584290487	0.002985718
Co	7.6	71.3	1.23	541.88	6.665124	0.177805854	0.002226841
Ni	7.45	22	4.38	163.9	7.17882	0.053780135	0.002358046
Cu	7.35	26592.6	0.16	195455.61	312.728976	64.13440566	0.148688826
Zn	7.25	41.6	42.61	301.6	128.51176	0.098963323	0.042127229
Sn Ka	6.25	4445.9	2.33	27786.875	647.4341875	9.117644222	0.193412524
Pb La	7	11245.6	0.23	78719.2	181.05416	25.82995242	0.075993738

953 keV

Element	H-value	Concentration	% Error	Adjusted Concentration	Adjusted Error	Normalized %	Error in %
Mn	6.04	6	18.66	36.24	6.762384	0.004511609	0.000842276
Fe	5.83	942.9	0.59	5497.107	32.4329313	0.684348774	0.005780396
Co	5.7	257.7	1.78	1468.89	26.146242	0.182865837	0.003434238
Ni	5.6	71.3	6.57	399.28	26.232696	0.049707379	0.003278129
Cu	5.5	93176.8	0.18	512472.4	922.45032	63.79898715	0.383413906
Zn	5.43	257.7	26.5	1399.311	370.817415	0.174203771	0.046095694
Sn Ka	4.95	14382	6.64	71190.9	4727.07576	8.862735464	0.536503915
Pb La	5.3	39773	0.35	210796.9	737.78915	26.24264002	0.171746872

AUGU

1701 keV

Element	H-value	Concentration	% Error	Adjusted Concentration	Adjusted Error	Normalized %	Error in %
Ti	9.21	4.6	7.51	42.366	3.1816866	0.011293067	0.000848202
Cr	8.38	2.5	9.69	20.95	2.030055	0.005584425	0.000541173
Fe	7.81	123.4	0.55	963.754	5.300647	0.256897944	0.001466735
Ni	7.45	120.2	1.11	895.49	9.939939	0.238701515	0.002670093
Cu	7.35	50676.2	0.14	372470.07	521.458098	99.28549748	0.075010192
Zn	7.25	17.4	194.05	126.15	244.794075	0.033626502	0.065230303
Se	6.93	5	33.48	34.65	11.60082	0.009236292	0.00309206
Sn Ka	6.25	28	79.4	175	138.95	0.046647942	0.037021257
Pb La	7	60.3	6.74	422.1	28.44954	0.112514835	0.007577054

953 keV

Element	H-value	Concentration	% Error	Adjusted Concentration	Adjusted Error	Normalized %	Error in %
Ti	7	21.3	5.09	149.1	7.58919	0.024319621	0.001260072
Cr	6.3	4.6	20.04	28.98	5.807592	0.004726912	0.000948349
Fe	5.83	372.1	1.12	2169.343	24.2966416	0.353840376	0.005243365
Ni	5.6	248.4	2.24	1391.04	31.159296	0.22689179	0.00553224
Cu	5.5	109561.9	0.74	602590.45	4459.16933	98.28820596	0.638107879
Zn	5.43	33.6	247.39	182.448	451.3581072	0.029758996	0.073599439
Se	5.28	32.5	35.56	171.6	61.02096	0.027989584	0.00995405
Sn Ka	4.95	1098.3	72.68	5436.585	3951.309978	0.886758471	0.63881386
Pb La	5.3	182.2	12.53	965.66	120.997198	0.157508286	0.019764413

TRAJ

1701 keV

Element	H-value	Concentration	% Error	Adjusted Concentration	Adjusted Error	Normalized %	Error in %
Ti	9.21	2.7	9.56	24.867	2.3772852	0.013762544	0.001317666
Cr	8.38	0.973	17.55	8.15374	1.43098137	0.004512656	0.000792319
Mn	8.02	0.919	19.6	7.37038	1.44459448	0.004079108	0.000799783
Fe	7.81	64.1	0.84	500.621	4.2052164	0.277066742	0.002771099
Ni	7.45	4	17.23	29.8	5.13454	0.016492694	0.002842652
Cu	7.35	24259.3	0.51	178305.855	909.3598605	98.68268087	0.210205427
Zn	7.25	76.7	21.25	556.075	118.1659375	0.307757543	0.065218586
Sn Ka	6.25	78.9	73.96	493.125	364.71525	0.27291811	0.201304119
Pb La	7	108.6	4.06	760.2	30.86412	0.420729729	0.017164287

953 keV

Element	H-value	Concentration	% Error	Adjusted Concentration	Adjusted Error	Normalized %	Error in %
Ti	7	26.5	4.48	185.5	8.3104	0.032157255	0.001476304
Cr	6.3	4.3	20.11	27.09	5.447799	0.004696173	0.000945545
Mn	6.04	6.1	16.79	36.844	6.1861076	0.006387072	0.001074257
Fe	5.83	402.4	1.27	2345.992	29.7940984	0.406688209	0.00658102
Ni	5.6	15.6	26.15	87.36	22.84464	0.015144247	0.00396257
Cu	5.5	103487.9	1.02	569183.45	5805.67119	98.67049756	0.076734331
Zn	5.43	352.5	21.73	1914.075	415.9284975	0.331813465	0.07194142
Sn Ka	4.95	0	0	0	0	0	0
Pb La	5.3	579.7	4.67	3072.41	143.481547	0.532616019	0.025317682

PTO2

1701 keV

Element	H-value	Concentration	% Error	Adjusted Concentration	Adjusted Error	Normalized %	Error in %
V	8.62	2.1	16.38	18.102	2.9651076	0.005171927	0.000847248
Cr	8.38	2.5	11.54	20.95	2.41763	0.005985629	0.000690915
Fe	7.81	1130.9	0.26	8832.329	22.9640554	2.523486731	0.009670062
Co	7.6	97.9	2.56	744.04	19.047424	0.212579838	0.005464746
Ni	7.45	10.3	12.77	76.735	9.7990595	0.021923974	0.002799787
Cu	7.35	38797.7	0.17	285163.095	484.7772615	81.47401284	0.206860345
Zn	7.25	91.3	28.51	661.925	188.7148175	0.189118743	0.053818435
As	7.01	406.7	2.79	2850.967	79.5419793	0.814550431	0.022661409
Ag Ka	6.33	56.6	19.68	358.278	70.5091104	0.102363689	0.020126694
Sn Ka	6.25	6629.4	1.96	41433.75	812.1015	11.83804615	0.205543224
Pb La	7	1406.4	2.69	9844.8	264.82512	2.812760051	0.073947711

953 keV

Element	H-value	Concentration	% Error	Adjusted Concentration	Adjusted Error	Normalized %	Error in %
V	6.62	4.7	20.2	31.114	6.285028	0.007232866	0.00146399
Cr	6.3	3.7	25.57	23.31	5.960367	0.005418722	0.001387302
Fe	5.83	2232.9	0.72	13017.807	93.7282104	3.026163618	0.044847297
Co	5.7	182.9	3.82	1042.53	39.824646	0.242350064	0.009763708
Ni	5.6	16.8	23.53	94.08	22.137024	0.021870156	0.005152861
Cu	5.5	62659.7	0.64	344628.35	2205.62144	80.11347645	0.968865056
Zn	5.43	282.4	18	1533.432	276.01776	0.35646681	0.064104523
As	5.3	504.8	12.15	2675.44	325.06596	0.621941867	0.075533426
Ag Ka	5	0	0	0	0	0	0
Sn Ka	4.95	10099	10.11	49990.05	5053.994055	11.62085677	1.04047568
Pb La	5.3	3233.8	5.92	17139.14	1014.637088	3.984222681	0.232191673

SELE

1701 keV

Element	H-value	Concentration	% Error	Adjusted Concentration	Adjusted Error	Normalized %	Error in %
V	8.62	90.6	0.92	780.972	7.1849424	0.336840236	0.003548714
Cr	8.38	3.9	12.09	32.682	3.9512538	0.01409604	0.00170554
Mn	8.02	8.6	3.28	68.972	2.2622816	0.029748243	0.000987589
Fe	7.81	111.8	0.76	873.158	6.6360008	0.376600886	0.003456691
Co	7.6	16.4	3.34	124.64	4.162976	0.053758351	0.001816112
Ni	7.45	36.3	2.24	270.435	6.057744	0.116641044	0.002678969
Cu	7.35	20772.4	0.49	152677.14	748.117986	65.85102142	0.289378891
Zn	7.25	19.2	74.54	139.2	103.75968	0.06003821	0.04472669
Sn Ka	6.25	6536.2	2.23	40851.25	910.982875	17.61951094	0.329146755
Pb La	7	5147.7	0.6	36033.9	216.2034	15.54174463	0.111784778

953 keV

Element	H-value	Concentration	% Error	Adjusted Concentration	Adjusted Error	Normalized %	Error in %
V	6.62	179.6	1.24	1188.952	14.7430048	0.456922552	0.010184589
Cr	6.3	4.6	28.9	28.98	8.37522	0.011137216	0.003224928
Mn	6.04	21.6	4.64	130.464	6.0535296	0.050138226	0.002504538
Fe	5.83	281.6	1	1641.728	16.41728	0.630927529	0.013282582
Co	5.7	24.8	7.83	141.36	11.068488	0.054325635	0.004369314
Ni	5.6	57.9	4.52	324.24	14.655648	0.124607695	0.006082102
Cu	5.5	31050.9	0.23	170779.95	392.793885	65.63192679	1.215191448
Zn	5.43	20.5	130.55	111.315	145.3217325	0.042779131	0.055829906
Sn Ka	4.95	9041.6	10.72	44755.92	4797.834624	17.20001244	1.527135674
Pb La	5.3	7755.8	0.87	41105.74	357.619938	15.79722279	0.314457779

REFERENCES

1. S. Johansson, J. Campbell, and K. Malmqvist, eds., *Particle-Induced X-Ray Emission Spectrometry (PIXE)*, (John Wiley & Sons, New York, 1995) 451 p.

2. J. Maxwell, J. Campbell, and W. Teesdale, "The Guelph PIXE Software Package", *Nuclear Instruments and Methods in Physics Research* **B43** (1988) 218.

3. S. Perry, *Design, Construction, and Testing of an External-Beam PIXE System for Coin and Manuscript Analysis at Brigham Young University* [Undergraduate Honors Thesis], (Brigham Young University, Provo, 1999) 69 p.

4. G. Demortier and M. Meyer, "Nonvacuum Analysis of Silver Coins (9^{th} to 15^{th} Century A.D.)", *Nuclear Instruments and Methods in Physics Research* **B49** (1990) 300.

5. I. Brissaud and others, "Analysis of Gaulish Coins by Proton Induced X-Ray Emission, Synchrotron Radiation X-Ray Fluorescence and Neutron Activation Analysis", *Nuclear Instruments and Methods in Physics Research* **B49** (1990) 305.

6. M. Araujo, L. Alves, and J. Cabral, "Comparison of EDXRF and PIXE in the analysis of ancient gold coins", *Nuclear Instruments and Methods in Physics Research* **B75** (1993) 450.

7. J. Condamin and M. Picon, in: *Methods of Chemical and Metallurgical Investigation of Ancient Coinage*, eds. E. Hall and D. Metcalf, Special Publication No. 8 (Royal Numismatic Society, London, 1972) pp. 49.

8. M. Jaksic and others, "PIXE Depth Profiling", *Nuclear Instruments and Methods in Physics Research* **B40/41** (1989) 643.

9. I. Brissaud, J. Frontier, and P. Regnier, "Evaluation of Depth Profiling with PIXE", *Nuclear Instruments and Methods in Physics Research* **B12** (1985) 235.

10. G. Demortier, Y. Morciaux, and D. Dozot, "PIXE, XRF and GRT for the global investigation of ancient gold artifacts", *Nuclear Instruments and Methods in Physics Research* **B150** (1999) 640.

11. G. Demortier, S. Mathot, and B. Van Oystaeyen, "Complementarity of RBS, PIGE and PIXE for the Determination of Surface Layers of Thicknesses Up to 30 Microns", *Nuclear Instruments and Methods in Physics Research* **B49** (1990) 46.

12. H. Stanley and R. Froberg, "Unusual Structural Characteristics of a Unique Thin Pyrolytic Graphite Film", 10th Biennial Conference on Carbon, Lehigh University (1971).

Foil manufactured by Pfizer, Inc., Easton, PA.

13. D. Mingay, "Calibration of Micromatter Co. Standards Used for the Calibration of PIXE Analysis Systems", *Journal of Radioanalytical Chemistry* **78/1** (1983) 127.

Foils manufactured by Micromatter Co., Deer Harbor, WA.

14. http://www.pleo.com/Dupont/kap_thick.htm (May, 2003).